Applied Clay Science 245 (2023) 107144

Contents lists available at ScienceDirect

Applied Clay Science

journal homepage: www.elsevier.com/locate/clay

Research Paper

High-pressure Raman scattering and X-ray diffraction study of kaolinite, $Al_2Si_2O_5(OH)_4$

Abhisek Basu [a,*], Mainak Mookherjee [a], Stephen Clapp [a], Stella Chariton [b], Vitali B. Prakapenka [b]

[a] Earth Materials Laboratory, Department of Earth, Ocean and Atmospheric Sciences, Florida State University, Tallahassee, FL 32306, USA
[b] Center for Advanced Radiation Sources, The University of Chicago, Chicago, IL 60637, USA

ARTICLE INFO

Keywords:
Kaolinite
Raman spectroscopy
X-ray diffraction
Hydrogen bonding
High-pressure
Equation of state

ABSTRACT

Kaolinite is formed by weathering of continental crustal rocks and is also found in marine sediments in the tropical region. Kaolinite and other layered hydrous silicate minerals are likely to play a vital role in transporting water into the Earth's interior via subducting slabs. Recent studies have experimentally documented the expansion of the interlayer region by intercalation of water molecules at high pressures i.e., pressure-induced hydration. This is counter-intuitive since the interlayer region in the layered silicates is quite compressible, so it is important to understand the underlying mechanism that causes intercalation and expansion of the interlayer region.

To address this, we explore the high-pressure behavior of natural kaolinite from Keokuk, Iowa. This sample is free of anatase impurities and thus helps to examine both low-energy (0–1200 cm^{-1}) and high-energy hydroxyl (3000–4000 cm^{-1}) regions using Raman spectroscopy and synchrotron-based powder X-ray diffraction.

Our results show that the pressure dependence of the hydroxyl modes exhibits discontinuities at ~3 GPa and ~ 6.5 GPa. This is related to the polytypic transformation of Kaolinite from K-1 to K-II and K-II to K-III phase. Several low-energy Raman modes' pressure dependence also exhibits similar discontinuous behavior. The synchrotron-based powder X-ray diffraction results also indicate discontinuous behavior in the pressure dependence of the unit-cell volume and lattice parameters. The analysis of the bulk and the linear compressibility reveals that kaolinite is extremely anisotropic and is likely to aid its geophysical detectability in subduction zone settings. The K-I to K-II polytypic transition is marked by the snapping of hydrogen bonds, thus at conditions relevant to the Earth's interior, water molecules intercalate in the interlayer region and stabilize the crystal structure and help form the super-hydrated kaolinite which can transport significantly more water into the Earth's interior.

1. Introduction

Kaolinite [$Al_2Si_2O_5(OH)_4$] is a naturally occurring clay mineral often produced by weathering of continental crustal rocks. It is quite likely that a minor amount of common aluminosilicate clays such as kaolinite might have been produced in the acidic environment of ancient active volcanoes on the earliest anoxic protocontinents in the Hadean Earth (<4.55 Ga) (Hazen et al., 2013). Following the moon-forming impact, i.e., post-Hadean Earth the alteration of granite is likely to have led to the first significant production of several dioctahedral aluminosilicate clays including kaolinite. This possibility of forming aluminosilicate clays including kaolinite in the Earth's early history is further supported by their presence in the ancient heavily cratered Noachian terrains (Bishop et al., 2008; Ehlmann et al., 2011). The presence of kaolinite on the Martian surface is likely to have formed in an open system with a high water-to-rock ratio (Ehlmann et al., 2011). In the context of the planet Earth, oxidative weathering probably became more likely after the Great Oxidation Event which assisted in clay formation (Lyons et al., 2009). Once formed, kaolinite might have played a vital role in absorbing and transporting phosphorus from the continents to the marine environment making the phosphorus bioavailable to phytoplankton, thus linking the Great Oxidation and the Lomagundi events (Hao et al., 2021). The abundance of kaolinite shows a positive correlation with the availability of oxygen in Russian platforms (Lisitzin and Rodolfo, 1972). In modern oceans, the distribution of kaolinite is correlated with climate, i.e., temperature and rainfall correlate positively with the latitudinal

---

* Corresponding authors.
E-mail addresses: abasu@fsu.edu (A. Basu), mmookherjee@fsu.edu (M. Mookherjee).

https://doi.org/10.1016/j.clay.2023.107144
Received 27 June 2023; Received in revised form 19 August 2023; Accepted 14 September 2023

abundance of kaolinite (Lisitzin and Rodolfo, 1972).

Aluminosilicate clays such as smectites and kaolinite are valuable industrial minerals and are often used in the synthesis of clay-polymer nanocomposites. Such industrial use is often related to the capacity of clay minerals to swell and exchange cations in the interlayer region. Although the cation exchange capacity of kaolinite is extremely low owing to the hydrogen-bonded interlayer region, it is now known that if the hydrogen bonding is weakened, kaolinite does participate in cation exchange reactions with several organic molecules including acetamide, dimethyl sulphoxide (DMSO), dimethyl acetamide, dimethyl formamide, formamide, hydrazine, N methyl acetamide, N methyl formamide, pyridine N oxide, and urea (Johnston, 2010). In a recent study, intercalation of water has been reported in kaolinite at high pressures and temperatures, a phenomenon referred to as pressure-induced hydration (PIH) (Hwang et al., 2017, 2019; Basu and Mookherjee, 2021). It is speculated that such pressure-induced hydration is likely to transport significantly more water into the Earth's interior. It is expected that at higher pressures the interlayer hydrogen bonding is likely to strengthen, and thus intercalation at high pressures, which requires breaking of hydrogen bonding, is counterintuitive. A key question is what structural changes does kaolinite undergo to facilitate such intercalation at high pressures? So far only a few studies examined the structural changes of kaolinite and its structural polytypes at high pressures (Johnston et al., 2002; Dera et al., 2003; Welch and Crichton, 2010; Welch et al., 2012; Hwang et al., 2017; Michalski et al., 2017; Basu and Mookherjee, 2021; Hong et al., 2022). The high-pressure studies based on X-ray diffraction have proposed polytypic transformations (Dera et al., 2003; Welch and Crichton, 2010). The high-pressure studies based on Raman and infrared spectroscopy have proposed changes in the hydrogen-bonded environment (Johnston et al., 2002; Welch et al., 2012; Basu and Mookherjee, 2021; Hong et al., 2022). However, we note that the naturally occurring kaolinites found in weathered deposits often occur together with trace amounts of (~5%) dispersed anatase (TiO_2) and iron oxides primarily due to the insolubility of Ti^{4+} and Fe^{3+} (Railsback, 2003). The trace quantities of minor phases are unlikely to affect the X-ray diffraction pattern, however, it is very likely to affect the low-energy region of the vibrational spectra. Also, naturally occurring kaolinites vary in crystallinity which significantly influences the proton environment and the hydroxyl region of the vibrational spectra. It is not known how crystallinity affects the high-pressure behavior of the crystal structure of kaolinite.

In this study, we want to build on these previous high-pressure-based studies and compare and/or contrast our results with existing literature. Our study is intended to shed insight into the high-pressure behavior of naturally occurring crystalline kaolinite with no traceable impurity phases. In this study, we use synchrotron-based X-ray diffraction and both low energy and hydroxyl region using Raman spectroscopy to explore the high-pressure behavior of highly crystalline kaolinite from Keokuk, Iowa.

2. Methods

Raman Scattering and X-ray diffraction has been successfully used to gain insight into a wide variety of hydrogen-bonded minerals and inorganic compounds at high pressures (Auzende et al., 2004; Basu et al., 2012; Basu and Mookherjee, 2021; Basu et al., 2023; Comodi et al., 2007; Dera et al., 2003; Duffy et al., 1995; Gonzales-Platas et al., 2019; Holtz et al., 1993; Huang et al., 1996; Hwang et al., 2019; Johnston et al., 2002; Kleppe et al., 2001; Koch-Müller et al., 2005; Meade and Jeanloz, 1990; Mookherjee et al., 2015; Welch and Crichton, 2010; Ye et al., 2013). Thus, in this study, we explore the high-pressure behavior of kaolinite using Raman scattering and X-ray diffraction.

At ambient conditions, we examined three distinct naturally occurring polycrystalline kaolinite using X-ray diffraction- (a) commercially obtained from Sigma Aldrich (SA), (b) from Warren County, West Georgia (KGa-I, obtained from Source Clays Repository, The Clay Minerals Society, often referred to as low defect kaolinite (LD)), and (c) from Keokuk, Iowa, USA (Keokuk). In a recent study, we examined SA and LD kaolinite (Basu and Mookherjee, 2021) and hence, at ambient conditions, we only examined Keokuk Kaolinite using Raman scattering.

For the X-ray diffraction and Raman scattering data at high pressures, we used Keokuk kaolinite owing to its high crystallinity. For the high-pressure X-ray diffraction and Raman scattering study, we used a symmetric diamond anvil cell (DAC). In the symmetric DAC, we used two low-fluorescence type-I diamonds with a culet size of 300 μm. We used a 150 μm thick stainless gasket. We pre-indented the gasket to 50 μm and drilled a 100 μm center hole using an Almax-Boehler μ-driller. We used a 4:1 methanol-ethanol mixture which is hydrostatic up to ~10 GPa, as a pressure media for both the XRD and Raman scattering measurements (Angel et al., 2007; Klotz et al., 2009). We carried out the high-pressure Raman and XRD measurements to ~8 GPa. This is well within the hydrostatic limit of the methanol-ethanol mixture (Angel et al., 2007; Klotz et al., 2009). For the Raman measurements, we used ruby fluorescence for the pressure calibration (Mao et al., 1986). The typical error associated in pressure measurements associated with ruby fluorescence method is around $< \pm 0.1$ GPa.

We have used a synchrotron-based powder X-ray diffraction (XRD) at the Advanced Photon Source, Argonne National Laboratory, Illinois, USA to characterize these three samples. We used beamline 13 ID-D of the GSECARS where the primary white beam from the wiggler source was focused on the cryo-cooled Si (111) crystal to produce a monochromatic X-ray with a wavelength of 0.3344 Å. The images from the Pilatus 1 M CdTe detector were corrected and integrated into 2θ versus intensity profiles using DIOPTAS (Prescher and Prakapenka, 2015). The high crystalline quality of all three samples was confirmed by the presence of sharp and well-defined $(1\overline{1}0)$, and $(11\overline{1})$ reflections (Supplementary Materials). The X-ray diffraction pattern is an average of multiple crystals with random orientations. We collected our X-ray diffraction patterns by rotating the symmetric DAC around the omega axis. During each of the data collection, the sample/symmetric DAC was constantly rotated over 70° with a total exposure time of ~280 s. This allowed us to sample a large portion of the reciprocal space. We carried out LeBail refinement of the lattice parameters using the GSAS-II (Toby and Von Dreele, 2013). The refined lattice parameters of the three kaolinites are in excellent agreement with the previous report (Welch and Crichton, 2010) (Supplementary Materials). We used the gold equation of state to determine pressures in the high-pressure X-ray diffraction study. The typical uncertainties in the pressures associated with the equation of state of gold is $<\pm 0.1$ GPa (Heinz and Jeanloz, 1984).

We collected the Raman spectra of the kaolinite samples at ambient conditions. We used a Horiba Jobin-Yvon LabRam HR Evolution spectrometer equipped with a thermoelectrically cooled CCD detector. We used a frequency-doubled Nd-YAG laser (λ=532 nm) with a maximum 300 mW output power at the source. For measurement at the ambient conditions, we focused the laser through a 100× magnification objective. The Raman spectrometer setup involves an 1800 lines/mm grating, setting the spectral resolution at 2 cm^{-1}. We optimized the laser power to obtain the best possible spectra and eliminate the likelihood of local heating and damage to the sample by the laser (Basu and Mookherjee, 2021).

For the three kaolinite samples, we explored the high-energy region (3550–3750 cm^{-1}) that is sensitive to the hydroxyl (O-H) stretching vibrations. Natural kaolinite samples often occur together with the anatase (TiO_2) mineral phase (Murad, 1997; Schroeder and Shiflet, 2000; Schroeder et al., 2003). Among the three kaolinite samples explored in this study, Keokuk is free from the effects of the anatase. Therefore, considering the crystallinity from the XRD measurements and the quality of the ambient Raman spectrum we explored the high-pressure behavior of Keokuk kaolinite using static compression. To improve the signal-to-noise ratio, we collected the Raman spectra for 20 s and averaged over 15 accumulations.

3. Results

3.1. Raman spectroscopy

The Raman spectroscopic data is well understood in terms of the crystal structure of kaolinite that has a layered crystal structure consisting of one tetrahedral (T) sheet attached to one octahedral (O) sheet, i.e., T:O has a 1:1 ratio. These T:O units are attached to an adjacent T-O unit with weak hydrogen bonds (O-H….O). The tetrahedral layers are composed of an infinite sheet of di-trigonal rings with a fundamental repeat unit of $(Si_2O_5)^{2-}$. Overall, kaolinite stoichiometry is intimately related to fundamental units- $(Si_2O_5)^{2-}$ and $Al(OH)_3$ connected to form $[O_3^bSi_2O_2^{nb}(OH)^IAl_2(OH)_3^{IS}]$, the superscript '*b*' refers to bridging oxygen ions or the basal oxygen ions, '*nb*' refers to non-bridging oxygen ions or the apical oxygen ions that are attached to octahedral layers, superscript "*I*" refers to "inner hydroxyl", and "*IS*" refers to "inner surface" or "outer" hydroxyls. The octahedral layer has a stoichiometry of gibbsite $(Al(OH)_3)$, and consists of two trivalent aluminum ions (Al^{3+}), i.e., di-octahedral (Pauling, 1930; Brindley and Robinson, 1946; Bish, 1993; Neder et al., 1999). Kaolinite crystal structure has triclinic *C*1 space group symmetry with 17 atoms in the primitive unit cell (Welch and Crichton, 2010). This translates to a total of 51 vibrational modes i.e. $\Gamma=$ 51 A. Among these, 51 A, 3 A modes are acoustic, i.e., $\Gamma_{acoustic}=3$ A and the remaining 48 A modes are both Raman and infrared active, i.e., Γ_{optic} = 48 A. However, in layered silicates such as kaolinite, the vibrational modes can be understood in terms of an ideal hexagonal lattice with $[O_3^bSi_2O_2^{nb}]$ units with $C_{6v}(6mm)$ point group symmetry, $Al(OH)_3$ octahedral units with $S_6(\overline{3})$ point group symmetry, and the *OH* ion that forms an isosceles triangular unit O-H-O with $C_{2v}(2mm)$ point group symmetry where the two oxygen ions are the two nearest non-bridged oxygen from the di-trigonal ring formed by the SiO_4 units (Loh, 1973). For this ideal $C_{6v}(6mm)$ symmetry for the $[O_3^bSi_2O_2^{nb}]$ units, factor group analysis predictions are for three modes at 127, 130, and 285 cm^{-1} (Ishii et al., 1967). However, the $[O_3^bSi_2O_2^{nb}]$ units are often distorted to a di-trigonal arrangement with a $C_{3v}(3m)$ point group symmetry. The lowering symmetry from the C_{6v} is not much and can readily account for the observed modes in Keokuk kaolinite at ~120 cm^{-1} (ν_1^{lat}), 130 cm^{-1} (ν_2^{lat}) and 133 cm^{-1} (ν_3^{lat}) with ν_2^{lat} being the most intense and ν_3^{lat} being the second most prominent mode at ambient condition (Table 1, Fig. 1). The ν_3^{lat} is thought to be related to the Al-O octahedral deformation (Kloprogge, 2017).

We note that the naturally occurring well-ordered LD and SA kaolinite samples have an intense mode at ~142–144 cm^{-1} (Table 1). These kaolinites contain anatase (TiO_2) mineral phase (Murad, 1997; Schroeder and Shiflet, 2000; Schroeder et al., 2003) which has a very intense band ~143–144 cm^{-1} ($E_g^{TiO_2}$) attributed to the symmetric bending mode of O-Ti-O. In addition, anatase (TiO_2) also exhibits intense modes at 397 cm^{-1} ($B_{1g}^{TiO_2}$), 515 cm^{-1} ($A_{1g}^{TiO_2}+B_{1g}^{TiO_2}$), 639 cm^{-1} ($E_g^{TiO_2}$), and an additional less intense mode at 197 cm^{-1} ($E_g^{TiO_2}$) (Table 1) (Sekiya et al., 2001). It is also known that $E_g^{TiO_2}$ stiffens upon compression (Balachandran and Eror, 1982; Ohsaka et al., 1979; Sekiya et al., 2001), and thus it has been speculated that the variation of the ~144 cm^{-1} modes observed in kaolinite minerals is indicative of the stress

Table 1
Deconvoluted Raman mode frequencies of three kaolinites (Keokuk, SA, and LD) collected at ambient conditions.

		This study						W1979	J1985	M1986	MH22	TS01	EM97	RRUFF
		Keokuk, Iowa		*SA*		*LD (KGa-I)*		Keokuk	KGa-I	Mesa Alta	Nanshu	Anatase		
		ν_i	$\sigma\nu_i$	ν_i	$\sigma\nu_i$	ν_i	$\sigma\nu_i$	ν_i	ν_i	ν_i	ν_i	ν_i	ν_i	ν_i
$\nu1$	O-Si-O symm bend	119.7	0.1	118.5	0.2	117.8	0.5	120.0						
$\nu2$	O-Si-O symm bend	129.9	0.0	129.9	0.1	129.9	0.1		130.0	130.0				
$\nu3$	Si_2O_5 out of plane	133.0	0.1					132.0						
	ν_2(e) AlO_6/E_g (TiO_2)			142.2	0.0	143.9	0.0		141.0	143.0	146.8	144.5	146.0	143.0
$\nu4$	$A_{1g}(\nu_1)$ AlO_6	196.7	0.4	196.6	0.3	197.4	0.3	200.0	201.0	197.0		197.2	199.0	197.3
$\nu5$		207.2	1.1					215.0						
$\nu6$	$B_2(\nu_3)$ O-H-O triangle	244.9	0.2	244.4	0.2	243.7	0.3	248.0	244.0	245.0				
$\nu7$		270.7	0.2	272.4	0.3	273.7	0.2	272.0	271.0	270.0				
$\nu8$		278.1	1.0											
$\nu9$	$A_1(\nu_1)$ O-H-O triangle	336.7	0.2	336.0	0.2	336.0	0.2	338.0	335.0	336.0	337.8			
	ν_2(e) SiO_4/E_g (TiO_2)			394.6	0.4	395.2	0.2		397.0	394.0	402.4	396.6	397.0	396.7
$\nu10$	ν_2(e) SiO_4	415.0	0.3	416.1	0.4			420.0		418.0				
$\nu11$	ν_2(e) SiO_4	433.1	0.2	430.2	0.4	429.9	0.5	434.0	431	431				
$\nu12$	$\nu_4(f_2)$ SiO_4	459.6	0.2	462.7	0.3	462.8	0.9	461.0	461.0	463.0				
$\nu13$	$\nu_4(f_2)$ SiO_4	476.5	0.3	475.9	0.2	475.7	0.5				473.6			
$\nu14$	$\nu_4(f_2)$ SiO_4	507.2	0.5	512.7	0.3	515.8	0.2		512.0	516.0	517.2	515.3	514.0	518.0
				528.7	2.2									
	Si-O-Al translation			637.1	0.1	637.6	0.1		637.0	638.0	644.2	638.6	638.0	638.5
$\nu15$	Si-O-Al translation	711.1	1.5	707.7	0.4	706.9	1.2		700.0	710.0	710.9			
$\nu16$		748.1	0.2	750.6	0.2	751.0	0.5	749.0	750.0	751.0	759.9			
$\nu17$	OH translation	790.3	0.2	790.6	0.2	790.6	0.5	791.0	790.0	790.0				
$\nu18$	Al_2OH_i libration	913.4	0.2	913.2	0.2	914.4	0.6	916.0	915.0	915.0	914.3			
$\nu19$	Al_2OH_{is} libration	928.1	1.8	933.4	1.3			935.0	940.0	938.0				
		1010.0	1.1											
	$A_1(\nu_1)$ Si-O	1041.8	1.2					1048.0						
	$A_1(\nu_1)$ Si-O					1109.9	1.3	1105.0						
$\nu20$		1128.3	2.1	1118.9	1.2	1122.7	0.9							
$\nu21$		3620.5	0.0	3620.8	0.1	3621.1	0.1	3620.0	3621.0	3620.0	3622.0			
$\nu22$		3652.3	0.1	3654.0	0.0	3654.6	0.7	3650.0	3652.0	3651.0	3659.9			
$\nu23$		3668.8	0.1	3669.7	0.4	3669.8	0.9	3668.0	3668.0	3669.0	3670.0			
$\nu24$		3684.4	0.0	3690.2	1.1	3690.1	0.5	3682.0	3688.0	3684.0				
$\nu25$		3694.2	0.1	3699.1	0.2	3698.0	0.3	3692.0	3695.0	3695.0	3701.8			

Note: Natural kaolinite samples for this study - Keokuk: Keokuk, Iowa; SA: Sigma Aldrich (Switzerland); LD- Low defect, Warren County, Georgia. MH22 (Hong et al., 2022) and kaolinite sample from Nanshu Diggings in Suzhou city, Jiangsu province, China. TS01 (Sekiya et al., 2001); EM97 (Murad, 1997). Raman modes, ν_i, and errors, $\sigma\nu_i$, are in units cm^{-1}. Errors represent 1σ uncertainties.

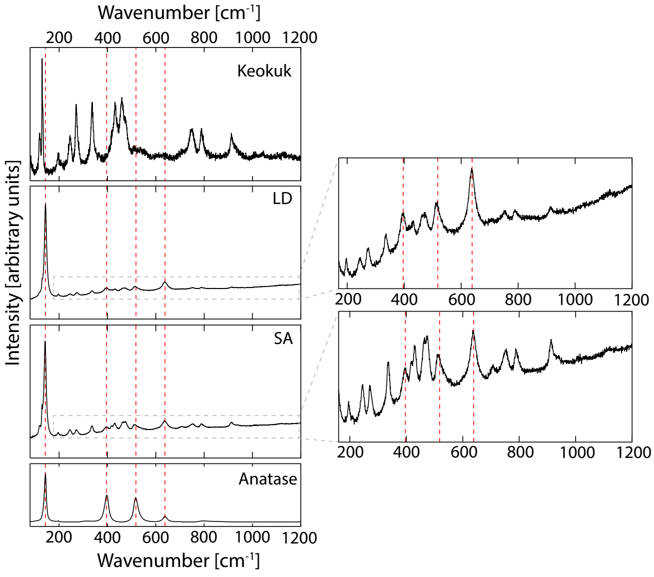

Fig. 1. Raman spectra of Keokuk, LD, SA, and anatase in the low wavenumber region from 100 cm^{-1} to 1200 cm^{-1}. The spectra were collected at ambient conditions on a glass slide with 100 x objective. The red dash lines indicate the vibrational modes of anatase impurities. The intense mode of anatase at ~144 cm^{-1} ($E_g^{TiO_2}$) attributed to the symmetric bending mode of O-Ti-O was observed in LD and SA kaolinites. The ~144 cm^{-1} ($E_g^{TiO_2}$) is absent in Keokuk kaolinite. The inset shows the zoomed in region to highlight the relatively less intense modes i.e., 397 cm^{-1} ($B_{1g}^{TiO_2}$), 515 cm^{-1} ($A_{1g}^{TiO_2}+B_{1g}^{TiO_2}$), 639 cm^{-1} ($E_g^{TiO_2}$) between wavenumber ~200 cm^{-1} and 1200 cm^{-1} for LD and SA kaolinite samples. (For interpretation of the references to colour in this figure legend, the reader is referred to the web version of this article.)

state or tension (Frost, 1995). Similar to the LD and SA kaolinite samples, an intense mode at ~147 cm^{-1} has been recently reported from the kaolinite sample from Nanshu Diggings in Suzhou City, Jiangsu province, China (Hong et al., 2022). The observed intense mode at ~147 cm^{-1} of Nanshu kaolinite is likely related to the $E_g^{TiO_2}$ and has been incorrectly characterized as O-Al-O symmetric bending mode (Hong et al., 2022). In addition, modes at 397 cm^{-1} ($B_{1g}^{TiO_2}$), 515 cm^{-1} ($A_{1g}^{TiO_2}+B_{1g}^{TiO_2}$); and 639 cm^{-1} ($E_g^{TiO_2}$) are observed in SA, LD, and Nanshu kaolinite samples (Table 1). Thus, it is likely that additional modes due to anatase may have been incorrectly identified as kaolinite vibrational modes (Hong et al., 2022) and further characterization of Nanshu kaolinite is necessary before high-pressure vibrational data could be interpreted and/or compared with high-pressure vibrational data of the Keokuk kaolinite from this study.

Upon compressing the sample, ~120 cm^{-1} (ν_1), 130 cm^{-1} (ν_2), and 133 cm^{-1} (ν_3) exhibit discontinuous pressure dependence at ~3.1 GPa. Upon slight compression, an additional mode in the high energy side of ν_1 mode and ~ 122 cm^{-1} (ν_{1a}) is also observed. Both these modes are broad and upon compression, these modes become untraceable above ~2.3 GPa. The pressure dependence of modes can be explained by a polynomial expression

$$\nu_i = \frac{d\nu_i}{dP}(P - P_{tr}) + \frac{d^2\nu_i}{dP^2}(P - P_{tr})^2 \tag{1}$$

where, P_{tr} is the transition pressure. The ν_2 mode exhibits modest pressure dependence with $\frac{\partial \nu_2}{\partial P}\sim$ 0.12 cm^{-1}/GPa. However, upon compression to ~3.1 GPa, there is an order of magnitude increase in the pressure dependence of ν_2 mode, i.e., $\frac{\partial \nu_2}{\partial P}\sim$ 1.81 cm^{-1}/GPa. This discontinuous change in the pressure dependence of ν_2 mode, i.e., $\frac{\partial \nu_2}{\partial P}$, coincides with the polytypic transition of kaolinite from the low pressure (K-I) to intermediate pressure (K-II) phase (Basu and Mookherjee, 2021; Welch and Crichton, 2010; Welch et al., 2012). The ν_3 exhibits discontinuous behavior across K-I to K-II transition and splits into two modes. And beyond ~6.2 GPa, which coincides with the intermediate pressure phase (K-II) to high-pressure phase (K-III), the ν_3 mode also exhibits discontinuous changes in its pressure dependence, $\frac{\partial \nu_3}{\partial P}$ (Fig. 2, Table 2).

The vibrational modes observed at 197 cm^{-1} (ν_4) and 210 cm^{-1} (ν_5) (Fig. 1, Table 1, Supplementary Materials) at ambient conditions can be attributed either due to the translational motion of the structural hydroxyl ions or due to the $[O_3^bSi_2O_2^{nb}]$ units with a reduced $C_{3v}(3m)$ point-group symmetry and is also seen (Michaelian, 1986). In some samples of kaolinite, the 197 cm^{-1} (ν_4) is observed around ~200 cm^{-1} and is also assigned to the $\nu_2(e)$ vibrational mode of the AlO$_6$ octahedral units (Frost and van der Gaast, 1997). We note that the observed mode 197 cm^{-1} (ν_4) coincides with the $E_g^{TiO_2}$ anatase which is often present as impurities in natural kaolinite. Does this mean that our Keokuk kaolinite sample also has impurities that we are unable to assess due to the overlapping modes of Keokuk kaolinite and anatase impurity? Three lines of evidence indicate that our sample does not have anatase impurity (a) the absence of intense mode between ~143–154 cm^{-1} ($E_g^{TiO_2}$) as reported in many other natural kaolinites; (b) at ambient condition, the $E_g^{TiO_2}$ mode in anatase is sharp but extremely weak, in contrast, the observed mode at 197 cm^{-1} (ν_4) is relatively strong and well-defined, (c) upon compression the ν_4 mode stiffens, i.e., $\frac{\partial \nu_4}{\partial P} > 0$, in contrast, the $E_g^{TiO_2}$ mode in anatase is known to soften upon compression, i.e., $\frac{\partial E_g^{TiO_2}}{\partial P} < 0$ (Sekiya et al., 2001) (Fig. 3).

The vibrational mode observed at 245 cm^{-1} (ν_6) (Fig. 1, Table 1, Supplementary Materials) at ambient conditions can be attributed to a mixture of silicon-oxygen deformation and hydroxyl libration (Michaelian, 1986). The vibrational modes observed at 271 cm^{-1} (ν_7) and 278 cm^{-1} (ν_8) have been attributed to mixed silicon-oxygen deformation and octahedral sheet vibrations (Michaelian, 1986).

The vibrational modes observed at 337 cm^{-1} (ν_9), 417 cm^{-1} (ν_{10}), 433 cm^{-1} (ν_{11}), 460 cm^{-1} (ν_{12}), 477 cm^{-1} (ν_{13}), and 509 cm^{-1} (ν_{14}) are attributed to the combination of Si-O deformation and vibrations associated with the octahedral sheet (Michaelian, 1986) (Fig. 1, Table 1, Supplementary Materials). We note that close to the 509 cm^{-1} (ν_{14}),

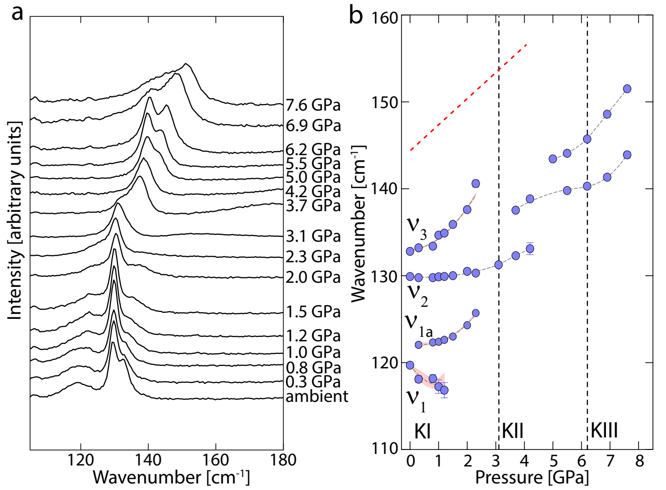

Fig. 2. (a) Raman spectra in the low energy region between 100 cm^{-1} and 180 cm^{-1}, collected at different pressures are stacked with an offset in the abscissa. (b) Deconvoluted vibrational modes in the the low energy region between 100 cm^{-1} and 180 cm^{-1} vs. pressure reveals discontinuous behavior across K-I to K-II and K-II to K-III phase. The red dashed line represents the pressure evolution of the $E_g^{TiO_2}$ mode, attributed to the symmetric bending of O-Ti-O unit of anatase. The pink shaded region represents a ± 1σ uncertainty.

Table 2
Pressure dependence of the low wavenumber modes in Keokuk kaolinite and coefficients of polynomial expansions.

	KI						KII						KIII					
i	ν_i^0	$\sigma\nu_i^0$	$\nu_i^{'}$	$\sigma\nu_i^{'}$	$\nu_i^{''}$	$\sigma\nu_i^{''}$	ν_i^0	$\sigma\nu_i^0$	$\nu_i^{'}$	$\sigma\nu_i^{'}$	$\nu_i^{''}$	$\sigma\nu_i^{''}$	ν_i^0	$\sigma\nu_i^0$	$\nu_i^{'}$	$\sigma\nu_i^{'}$	$\nu_i^{''}$	$\sigma\nu_i^{''}$
1	119.9	0.1	−4.43	1.41	2.18	1.50	131.3	0.0	1.81	0.83	−0.13	1.29	140.3	0.0	0.39	0.89	1.56	0.70
1a	122.4	0.3	−1.25	0.54	1.13	0.20	136.4	0.1	2.34	0.11	−0.36	0.03	145.7	0.1	4.05	0.25	0.06	0.19
2	129.9	0.0	−0.26	0.01	0.23	0.00	144.9	1.1	−2.24	0.87	0.86	0.17	195.8	0.7	6.50	2.24	−1.51	1.46
3	133.0	0.1	0.12	0.09	1.14	0.06	169.5	2.8	8.08	5.74	−2.36	2.04	220.1	0.4	14.35	3.84	−1.70	2.90
4	196.7	0.4	1.01	0.16	−0.04	0.07	197.7	0.2	6.54	0.30	0.27	0.10	248.7	0.3	9.72	0.79	−0.04	0.44
5	210.4	0.5	1.36	0.71	−0.53	0.18	221.8	0.5	5.46	0.48	−0.56	0.13	271.1	0.1	3.99	0.47	−0.82	0.34
6	244.9	0.2	0.27	0.41	−0.02	0.16	244.4	0.5	1.68	0.79	−0.06	0.23	288.9	0.1	6.80	0.28	−0.81	0.22
7	248.7	0.3	3.79	0.42	−0.38	0.12	257.4	0.2	5.14	0.24	−0.28	0.06	311.9	0.1	5.01	0.24	−0.49	0.17
8	270.7	0.2	5.58	0.04	−0.74	0.02	280.4	0.1	2.18	0.19	0.18	0.06	350.7	0.2	−0.02	0.42	1.02	0.23
9	278.1	1.0	9.43	0.10	−1.99	0.04	288.9	0.1	12.53	0.12	−1.68	0.03	429.2	–	4.18	–	−3.33	–
10	319.2	2.2	3.58	2.18	−0.64	0.50	342.2	0.0	−0.13	0.28	0.91	0.10	444.5	–	−0.49	–	0.49	–
11	336.7	0.2	2.56	0.03	−0.20	0.01	353.2	0.6	3.62	0.86	−0.41	0.27	492.3	–	−6.51	–	6.73	–
12	336.8	3.8	13.28	3.80	−2.65	0.89	420.4	1.2	6.05	1.86	−1.11	0.58	529.8	–	−3.13	–	4.43	–
13	417.3	0.4	1.38	0.54	−0.19	0.17	431.9	0.3	5.86	0.47	−0.60	0.15	656.6	1.7	0.46	5.43	0.42	3.32
14	433.1	0.2	−1.24	0.81	0.25	0.33	466.2	1.2	10.65	1.86	−2.28	0.58	689.3	3.1	−4.89	7.45	5.29	4.29
15	459.6	0.2	2.82	1.00	−0.06	0.41	485.7	0.8	16.29	1.23	−4.56	0.38	720.1	1.2	−2.23	3.21	0.93	1.87
16	476.5	0.3	6.13	1.31	−1.00	0.54	518.1	1.2	7.75	1.79	−1.36	0.56	769.8	0.1	0.33	0.19	1.43	0.11
17	509.4	0.8	3.86	1.16	−0.39	0.36	656.0	1.0	−10.82	2.26	5.23	0.90	828.0	1.0	6.49	2.59	−1.08	1.49
18	704.0	0.7	6.95	0.89	−0.87	0.25	717.4	0.5	1.61	0.97	0.46	0.38	833.1	5.0	3.30	0.68	–	–
19	748.1	0.2	4.92	0.05	−0.12	0.02	756.9	0.1	7.58	0.16	−1.10	0.04	908.2	0.7	1.73	2.43	1.49	1.76
20	790.3	0.2	1.53	0.05	1.02	0.02	802.4	0.6	7.81	0.64	−1.25	0.16	926.7	0.2	4.51	0.72	−0.80	0.49
21	800.4	1.2	−0.89	1.38	1.66	0.35	824.6	4.1	1.29	3.80	0.01	0.85	1031.5	1.0	5.88	7.24	−8.82	5.07
22	880.4	0.4	4.69	0.51	−0.10	0.15	894.4	0.3	2.86	0.69	0.57	0.23	1053.2	0.2	−1.34	1.00	0.36	0.70
23	913.4	0.2	1.89	0.14	0.26	0.06	922.3	0.3	−3.98	0.33	1.77	0.10	1101.7	1.0	−19.06	7.57	9.77	5.41
24	928.1	0.2	12.55	2.73	−4.11	2.04	1002.1	1.8	4.61	3.01	−1.56	1.03	1138.8	11.9	−4.81	30.70	3.85	19.60
25	1010.0	1.1	2.52	0.74	0.95	0.27	1041.6	1.0	−6.25	2.04	0.97	0.60						
26	1028.7	0.9	0.91	1.23	1.13	0.36	1058.8	0.5	−0.38	0.61	−0.45	0.16						
27	1041.8	1.2	8.53	0.31	−0.95	0.14	1113.3	0.7	−9.42	1.08	2.05	0.35						
28	1092.4	1.6	−2.61	2.07	1.21	0.57	1164.1	196.0	−8.82	245.00	1.82	69.90						
29	1102.9	0.7	8.55	0.98	−1.51	0.28	1096.2	1.2	−4.77	3.96	11.09	3.24						
30	1128.3	2.1	−0.65	0.62	1.21	0.23												
*	939.4	4.2	38.44	19.40	−16.33	14.70												

Note: Subscript "*i*" refers to the vibrational modes for K-I, K-II, and K-III. The pressure dependence of the modes is described by a polynomial expansion of the form $\nu_i(P_{ref}) + \nu_i^{'}(P - P_{ref}) + \nu_i^{''}(P - P_{ref})^2$, where $\nu_i\ [cm^{-1}]$ is the hydroxyl mode frequency at the reference pressure, $\nu_i^{'}\ [cm^{-1}/GPa]$ and $\nu_i^{''}[cm^{-1}/GPa^2]$ refers to the first derivative, $\frac{d\nu_i}{dP}$, and second derivative, $\frac{d^2\nu_i}{dP^2}$, respectively. The reference pressure, P_{ref}, refers to ambient conditions, i.e., 1 bar or 1×10^{-4} GPa for K-I, P_{ref} refers to ~3.1 GPa for K-II, and P_{ref} refers to ~6.2 GPa for K-III. Errors represent 1σ uncertainties.

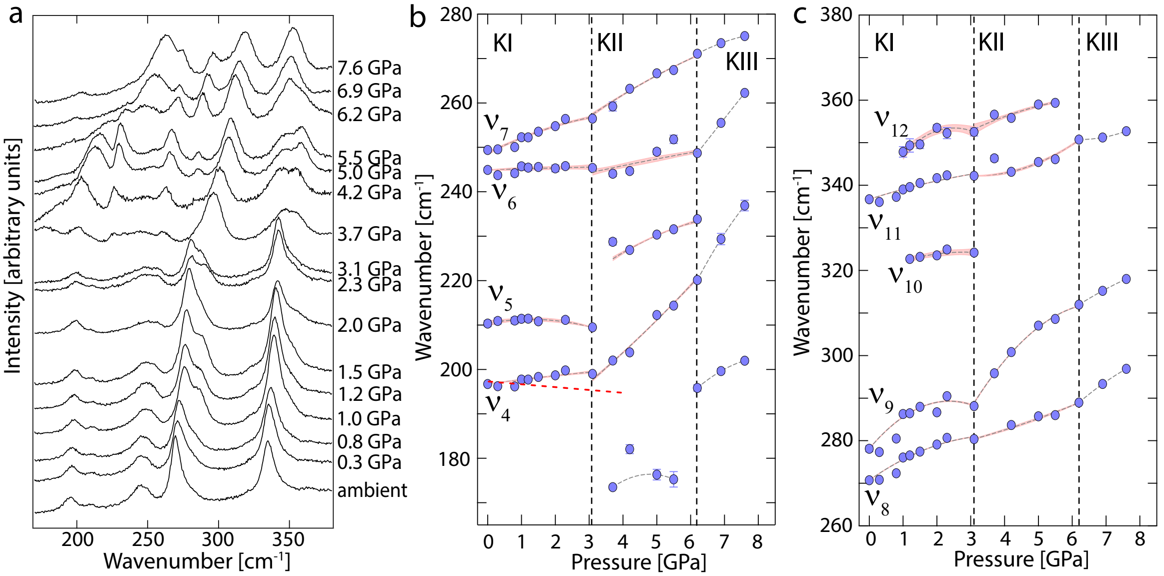

Fig. 3. (a) The plot shows the Raman Spectra in the low energy region between 180 cm^{-1} and 370 cm^{-1}, collected at different pressures are stacked with an offset in the abscissa. (b) Deconvoluted vibrational modes in the the low energy region between 180 cm^{-1} and 270 cm^{-1} vs. pressure reveals discontinuous behavior across K-I to K-II and K-II to K-III phase. The red dashed line represents the pressure evolution of the ~197 cm^{-1} $E_g^{TiO_2}$ mode, attributed to anatase, with distinct $\frac{\partial E_g^{TiO_2}}{\partial P} < 0$ (Sekiya et al., 2001) compared to the pressure dependence of the low energy mode $\frac{\partial \nu_4}{\partial P} > 0$ of Keokuk kaolinite. (c) Deconvoluted vibrational modes in the low energy region between 260 and 380 cm^{-1} vs. pressure reveals discontinuous behavior across K-I to K-II and K-II to K-III phase. The pink shaded region represents a ± 1σ uncertainty.

anatase also has a vibrational mode 515 cm^{-1} ($A_{1g}^{TiO_2} + B_{1g}^{TiO_2}$), but there remains a clear distinction between the ν_{14} and the $A_{1g}^{TiO_2} + B_{1g}^{TiO_2}$.

The vibrational modes observed at 711 cm^{-1} (ν_{15}), 748 cm^{-1} (ν_{16}), and 790 cm^{-1} (ν_{17}), are attributed to the combination of Si-O-Al vibrations and associated translations of the OH groups (Michaelian, 1986; Frost and Kloprogge, 1999) (Table 1). The vibrational modes observed at 913 cm^{-1} (ν_{18}) and 928 cm^{-1} (ν_{19}) are attributed to the in-plane bending motions $\left(\delta Al_2(OH)^I\right)$ and $\left(\delta Al_2(OH)^{IS}\right)$, where superscript "*I*" and "*IS*" refers to the inner hydroxyl and inner surface hydroxyl respectively (Farmer 1974). We observed vibrational modes at 1010 cm^{-1} (ν_{20}), 1042 cm^{-1} (ν_{21}), and 1128 cm^{-1} (ν_{22}). These modes are extremely weak and are observed at ambient conditions within the diamond anvil cells. Upon slight compression, the modes become more distinct. These modes are attributed to the Si-O stretching, i.e., ν (Si-O-Si).

The crystal structure of kaolinite has four proton sites: H1, H2, H3, and H4, that form distinct hydrogen-bonded environments (Bish, 1993). The H1 proton forms an "*inner hydroxyl*" group [Oh1-H1] that is approximately parallel to the (001) plane. The H1 proton is located within the cavity in the di-octahedral layer. The H2, H3, and H4 protons form the "inner surface" or "outer" hydroxyl groups [Oh2-H2], [Oh2-

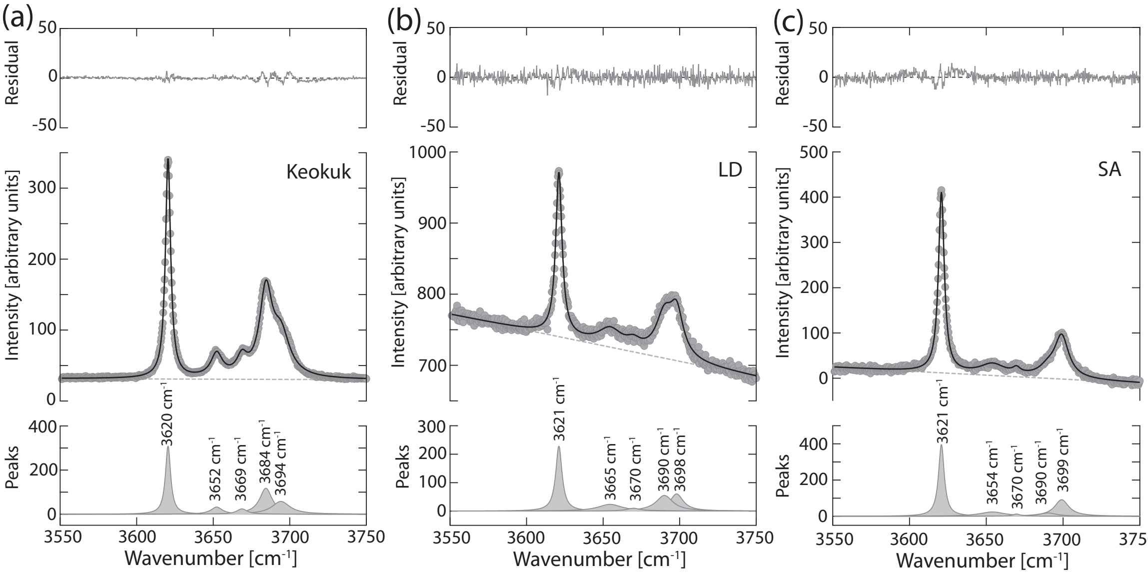

Fig. 4. Raman spectra of the hydroxyl stretching region between 3550 cm^{-1} and 3750 cm^{-1} collected at ambient condition on a glass slide. The spectra were collected with a 100× magnification objective. (a) Keokuk: kaolinite from Iowa, USA, (b) LD: low defect kaolinite from Warren County, Georgia, USA, and (c) SA: naturally occurring kaolinite obtained from Sigma Aldrich. The laser power used for the Raman measurements for all the three samples was 15 mW at the source.

H2], and [Oh2-H2] and are near vertical to the (001) plane (Bish, 1993). In the energy region between 3550 cm^{-1} and 3750 cm^{-1} we find five distinct modes at ~3621 cm^{-1} (ν_1^{OH}), 3652 cm^{-1} (ν_2^{OH}), 3669 cm^{-1} (ν_3^{OH}), 3685 cm^{-1} (ν_4^{OH}), and 3695 cm^{-1} (ν_5^{OH}) (Fig. 4, Table 1). The hydroxyl modes observed for Keokuk kaolinite are in good agreement with the LD and SA kaolinite with slight differences observed for the ν_4^{OH} and ν_5^{OH}, but the differences are $\Delta\nu \leq 5$ cm^{-1}. These slight differences in the energy of the hydroxyl modes may be attributed to slight differences in the crystallinity/crystal structure and the hydrogen bonding environment. Infrared spectra of kaolinite often exhibit four distinct O-H stretching modes (Farmer and Russell, 1964; Ledoux and White, 1966), the lowest energy mode ν_1^{OH} corresponds to the Oh1-H1 i.e., the '*inner hydroxyl*' mode. The higher energy O-H stretching modes (ν_2^{OH}, ν_3^{OH}, ν_4^{OH} and ν_5^{OH}), are related to the three hydroxyl groups i.e., Oh2-H2, Oh3-H3, and Oh4-H4 attached to an Al octahedral site. In an idealized crystal structure of kaolinite, these three O-H would be related by a three-fold symmetry and would result in two O-H modes: one would be due to an in-phase stretching mode where all the three Oh2-H2, Oh3-H3, and Oh4-H4 would vibrate in phase and perpendicular to the (001) layer and the other mode would be an out-of-phase vibration of the Oh2-H2, Oh3-H3, and Oh4-H4 modes (Farmer, 1964; Farmer and Russell, 1964; Farmer, 1974). However, the kaolinite crystal structure has lower symmetry than the ideal three-fold, and the out-of-phase vibrational mode is split into two modes (ν_2^{OH}, ν_3^{OH}) (Farmer and Russell, 1964; Farmer, 1974). Most infrared spectroscopic studies on kaolinite have characterized the OH stretching region into these four vibrational modes (Welch et al., 2012) and are consistent with theoretical predictions (Balan et al., 2001; Tosoni et al., 2006). However, an additional mode (ν_4^{OH}) has been observed in most kaolinite Raman spectra (Johnston, 1985; Michaelian, 1986; Frost and van der Gaast, 1997; Frost and Kloprogge, 1999; Basu and Mookherjee, 2021). The origin of the ν_4^{OH} in naturally occurring kaolinite samples or related to the LO-TO splitting due to the translational motion of the Oh2-H2 hydroxyls (Johnston, 1985). The reason that the ν_4^{OH} mode is not seen in the infrared spectra but observed in the Raman spectra is often attributed to the presence of an inversion center i.e. if the outer hydroxyls groups are attached to the adjacent tetrahedral layer such that Al-O-H…O-Si forms a linear geometric configuration, then such a configuration and the associated hydroxyl vibration could account for the ν_4^{OH} mode (Frost and van der Gaast, 1997).

Upon compression, the crystallographic environment of the proton is significantly altered. This is revealed in the changes in the OH-stretching modes. Similar to the low energy modes (100–1200 cm^{-1}), the pressure evolution of the inner hydroxyl, ν_1^{OH} and the inner surface hydroxyl, ν_2^{OH}, ν_3^{OH}, ν_4^{OH}, and ν_5^{OH} of Keokuk kaolinite also exhibits a transition from K-I to K-II at 3 GPa and K-II to K-III at 6 GPa and the pressure evolution can be adequately described by

$$\nu_i^{OH} = \frac{d\nu_i^{OH}}{dP}(P - P_{tr}) + \frac{d^2\nu_i^{OH}}{dP^2}(P - P_{tr})^2 \tag{2}$$

where, P_{tr} is the transition pressure. The pressure evolution of the modes is in good agreement with other kaolinite samples LD and SA (Basu and Mookherjee, 2021) (Fig. 5, Table 3).

Upon compression, we observe softening of all the ν_i^{OH} modes i.e., $\frac{d\nu_i^{OH}}{dP} < 0$ (Fig. 5). This is interpreted as the strengthening of the O-H….O, hydrogen bonds, and is consistent with prior observations on other kaolinite varieties (Basu and Mookherjee, 2021). Upon compression >3 GPa, i.e., in the intermediate phase of kaolinite (K-II), the ν_1^{OH}, ν_2^{OH}, and ν_3^{OH} modes stiffen. This compression-induced stiffening is in agreement with the previous study on other kaolinite varieties (Basu and Mookherjee, 2021). Upon further compression, i.e., beyond 6 GPa, the hydroxyl stretching modes show significant changes owing to the densification of the kaolinite structure to the K-III polymorph (Welch and Crichton, 2010; Welch et al., 2012). Four distinct modes are observed in the high-pressure polymorph (K-III) of kaolinite. This is consistent with prior studies (Basu and Mookherjee, 2021).

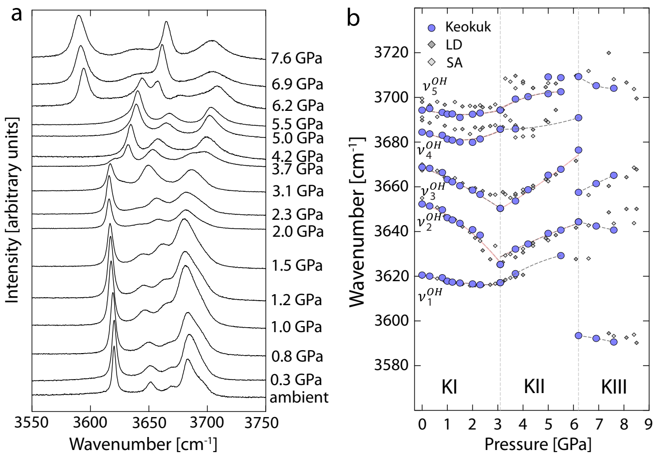

Fig. 5. (a) Raman Spectra in the hydroxyl region between 3550 cm^{-1} and 3750 cm^{-1}, collected at different pressures are stacked with an offset in the abscissa. (b) Deconvoluted vibrational modes in the hydroxyl stretching region between 3550 cm^{-1} and 3750 cm^{-1} vs. pressure reveals discontinuous behavior across K-I to K-II and K-II to K-III phase. Results from this study are in good agreement with prior study that explored pressure dependence of hydroxyl modes of LD and SA (Basu and Mookherjee, 2021). The pink shaded region represents a ± 1σ uncertainty (Table 3). (For interpretation of the references to colour in this figure legend, the reader is referred to the web version of this article.)

3.2. Synchrotron X-ray powder diffraction

The pressure-dependent synchrotron powder X-ray diffraction data of Keokuk kaolinite exhibit distinct changes around ~3.5 GPa i.e., the transformation from the low-pressure K-I phase to intermediate pressure K-II phase and at ~6.5 GPa indicating transformation from the intermediate pressure K-II phase to the high-pressure K-III phase (Fig. 6). Our observation is in good agreement with a prior static compression of the X-Ray diffraction studies (Welch and Crichton, 2010) (Supplementary Materials). Our finite strain analysis for bulk and linear compressibility (Angel, 2000; Birch, 1978, Davies, 1974; Gonzalez-Platas et al., 2016; Weaver, 1976; Supplementary Materials) of the X-ray diffraction data up to 3 GPa, i.e., K—I phase yields K_0~66.39 (±5.5) GPa, K'_0~1.24 (±4.28), K_a~396.01 (±18.1) GPa, K_b~288.07 (±18.8) GPa, and K_{c^*}~107.29 (±14.4) GPa. When we combine data from our study and prior study (Welch and Crichton, 2010), finite strain analysis of the K—I phase yields K_0~62.14 (±3.68) GPa, K'_0~2.26 (±2.98), K_a~389.80 (±12.8) GPa, K_b~251.35 (±11.7) GPa, and K_{c^*}~117.21 (±8.94) GPa. We find that K_a: K_b: K_{c^*} is 3.33:2.14:1.00. While our bulk modulus is in good agreement with the prior estimate of K_0~59.07 (±0.70) GPa, the linear moduli are quite distinct i.e., K_a~88.60 (±3.5) GPa, K_b~85.40 (±2.8) GPa, and K_{c^*}~34.6 (±0.50) (Welch and Crichton, 2010). The likely difference between our estimates and that of the prior study (Welch and Crichton, 2010) is the formalism used in the prior study where the lattice parameters were cubed to obtain a fictitious volume, and a bulk finite strain formalism was used to determine linear compressibility. The bulk modulus determined in this study using the linear compressibility is ~65.29 GPa i.e., within ~1.7% of the bulk modulus determined using the pressure-volume relationship using formalism (Supplementary Materials). In contrast, the bulk modulus determined from prior estimates (Welch and Crichton, 2010) using the linear compressibility is ~19.26 GPa i.e., ~68% discrepancy between the bulk modulus determined using the Birch Murnaghan finite strain formalism for volume. The linear compressibility can also be determined using the full elastic constant tensor and its compliance (Nye, 1985;

Table 3
Pressure dependence of the hydroxyl vibrational modes in kaolinite and coefficients of polynomial expansions.

KI							KII							KIII						
i	ν_i^{OH}	$\sigma\nu_i^{OH}$	$\nu_i^{'}$	$\sigma\nu_i^{'}$	$\nu_i^{''}$	$\sigma\nu_i^{''}$	i	ν_i^{OH}	$\sigma\nu_i^{OH}$	$\nu_i^{'}$	$\sigma\nu_i^{'}$	$\nu_i^{''}$	$\sigma\nu_i^{''}$	i	ν_i^{OH}	$\sigma\nu_i^{OH}$	$\nu_i^{'}$	$\sigma\nu_i^{'}$	$\nu_i^{''}$	$\sigma\nu_i^{''}$
										Keokuk [This study]										
1	3620.7	0.0	−3.10	0.01	0.54	0.00	1	3617.1	0.021	7.382	0.183	−0.97	0.099	1	3593.4	0.1	−1.56	0.27	−0.36	0.14
2	3652.3	0.1	−3.32	0.13	−1.66	0.05	2	3628.6	0.039	5.929	0.056	−0.34	0.017	2	3644.3	0.0	−2.73	0.54	0.08	0.42
3	3668.7	0.1	−4.35	0.09	−0.51	0.02	3	3650.1	0.029	6.634	0.068	0.379	0.027	3	3657.5	0.0	5.79	0.09	−0.24	0.06
4	3684.9	0.1	−5.24	0.19	1.71	0.06	4	3685.8	0.313	−0.13	0.987	0.574	0.303							
5	3694.7	0.1	−2.92	0.19	0.90	0.06	5	3694.9	0.179	6.334	0.247	−1.33	0.077	5	3709.3	0.1	−7.77	0.41	2.90	0.25
										SA & LD [BM21]										
1	3620.1	0.1	−3.16	0.11	0.58	0.04	1	3616.9	0.6	4.02	1.3	−0.18	0.46	1	3592.2	11.8	3.40	17.00	−1.98	5.70
2	3652.3	2.2	−1.76	4.18	−2.86	1.33	2	3627.8	0.2	4.44	0.21	0.01	0.07	2	3642.0	1.5	7.38	5.77	−2.47	3.10
3	3669.5	2.5	−7.44	3.31	1.01	0.96	3	3655.8	1.0	0.9	1.46	1.39	0.43	3	3656.0	2.5	7.17	3.64	−0.40	1.28
4	3690.2	1.5	−5.21	2.4	1.47	0.77	4	3691.9	2.0	−9.75	3.97	4.35	1.75							
5	3697.9	0.7	−1.74	1.15	0.43	0.39	5	3703.2	1.5	−0.38	1.57	0.79	0.37	5	3712.3	4.6	5.30	8.41	−5.38	3.53
										Nanshu Diggings [MH22]										
1	3622		6.40				1	3635.1		1.9				1	3643.9		13.30			
2	3659.9		−1.36				2	3664.2		6.74				2	3687.4					
3	3670		−1.71				3	3670.7		6.34				3	3696.0					
4	3701.8		−3.31				4	3701.8		3.13				4	3715.4					

Note: Subscript "i" refers to the vibrational modes 1–5 for K-I, K-II, and K-III. The pressure dependence of the modes is described by a polynomial expansion of the form $\nu_i^{OH}(P_{ref}) + \nu_i^{'}(P - P_{ref}) + \nu_i^{''}(P - P_{ref})^2$, where $\nu_i^{OH}\ [cm^{-1}]$ is the hydroxyl mode frequency at the reference pressure, $\nu_i^{'}\ [cm^{-1}/GPa]$ and $\nu_i^{''}[cm^{-1}/GPa^2]$ refers to the first derivative, $\frac{d\nu_i^{OH}}{dP}$, and second derivative, $\frac{d^2\nu_i^{OH}}{dP^2}$, respectively. The reference pressure, P_{ref}, refers to ambient conditions, i.e., 1 bar or 1×10^{-4} GPa for K-I, P_{ref} refers to ~3.1 GPa for K-II, and P_{ref} refers to ~6.2 GPa for K-III. Errors represent 1σ uncertainties. BM21 (Basu and Mookherjee, 2021). MH22 (Hong et al., 2022).

Supplementary Materials). And our estimates of the linear bulk moduli of kaolinite from the synchrotron-based powder X-ray diffraction analysis are consistent with the full elastic constant tensor determined using *first principles* simulation (Weck et al., 2015).

4. Discussion

The X-ray diffraction results clearly indicate that kaolinite is extremely anisotropic with K_{100} ~3.33 K_{001}i.e., the compression along the (100) plane is more than three times stiffer than that of the compression perpendicular to the (100) plane along the [001] direction. This is similar to many other geologically relevant layered hydrous phases. Although the volumetric abundances of hydrous phases are likely to be low in subducted slab and are likely to be confined to the hydrated regions and subsequent rehydration in the mantle wedge overlying the slab, owing to their extreme elastic anisotropy, these hydrous phases are likely to have unique geophysical signatures such as large delay time between arrivals of the two transverse shear waves. This also serves as a diagnostic feature for the layered hydrous phases and helps in their detectability in subducting slab and mantle wedges.

When we compare several layered hydrous silicates and their compressibility and anisotropy, we do not find any correlation between the linear compressibility K_a, K_b, vs. K_o of layered hydrous phases. However, we find a linear correlation between the bulk modulus, K_0, and the linear compressibility, K_{c^*} for layered hydrous silicates (Fig. 7). In our analysis, most of the linear compressibility for the layered hydrous phases was determined from the full elastic constant tensors. Very few layered hydrous silicates have been examined using Brillouin scattering and thus our analysis also relies on full elastic constant tensor predictions from the *first principles* simulation based on density functional theory that are often dependent on the approximations and whether dispersive corrections were used (Fig. 7, Supplementary Materials).

With the faster compression along the [001] direction, the near perpendicular hydroxyl (OH) units are often pulled towards the overlying oxygen ions from the basal oxygen ions of the overlying tetrahedral units, i.e., the O-H….O hydrogen bonds are strengthened. This is manifested in the pressure-induced lowering of the ν_{OH} modes i.e., $\frac{d\nu^{OH}}{dP} < 0$, often known as red-shift. A similar red shift is observed for many hydrous minerals and can be interpreted as strengthening of the hydrogen bonds O-H…O, where the hydroxyl group (O-H) is stretched. We note that the pressure-induced hydrogen bonding in layered hydrous silicates and oxides is dependent on the balance between the attractive forces that the hydrogen ion feels from the nearby oxygen ion and the repulsive forces due to interlayer cations and/or octahedral cations. The $\frac{d\nu^{OH}}{dP}$ vs. ν^{OH} for layered hydrous silicates could be explained by a linear trend, $\frac{d\nu^{OH}}{dP} = a\nu^{OH} + b$, with $a\sim -229.25$, $b\sim 0.06284$ i.e., $\frac{d\nu^{OH}}{dP} = 0$ at $\nu^{OH}\sim$ 3648.4 cm^{-1} (Fig. 7). This is in good agreement with prior estimates of 3625 cm^{-1} (Hofmeister et al., 1999), which is considered the limit of hydrogen bonding. We note that di-octahedral sheet silicates and oxides i.e., gibbsite, kaolinite, and muscovite often exhibit $\frac{d\nu^{OH}}{dP} < 0$ even for $\nu^{OH} >$ 3648.4 cm^{-1}. In contrast, for $\nu^{OH} >$ 3648.4 cm^{-1} the tri-octahedral sheet silicates in general exhibit $\frac{d\nu^{OH}}{dP} > 0$, with brucite and 10 Å phase being notable exceptions (Fig. 7). Similar to the layered hydrous silicates and oxides, the humite group of minerals, dense hydrous magnesium silicates, and nominally anhydrous minerals show similar trends for $\frac{d\nu^{OH}}{dP}$ vs. ν^{OH}.

5. Conclusion

Among kaolinite samples investigated at high-pressures, i.e., commercially obtained from Sigma Aldrich (SA), Warren County, West Georgia (KGa-I) often referred to as the low defect (LD) kaolinite, and kaolinite from Nanshu diggings in China, we find that Keokuk kaolinite

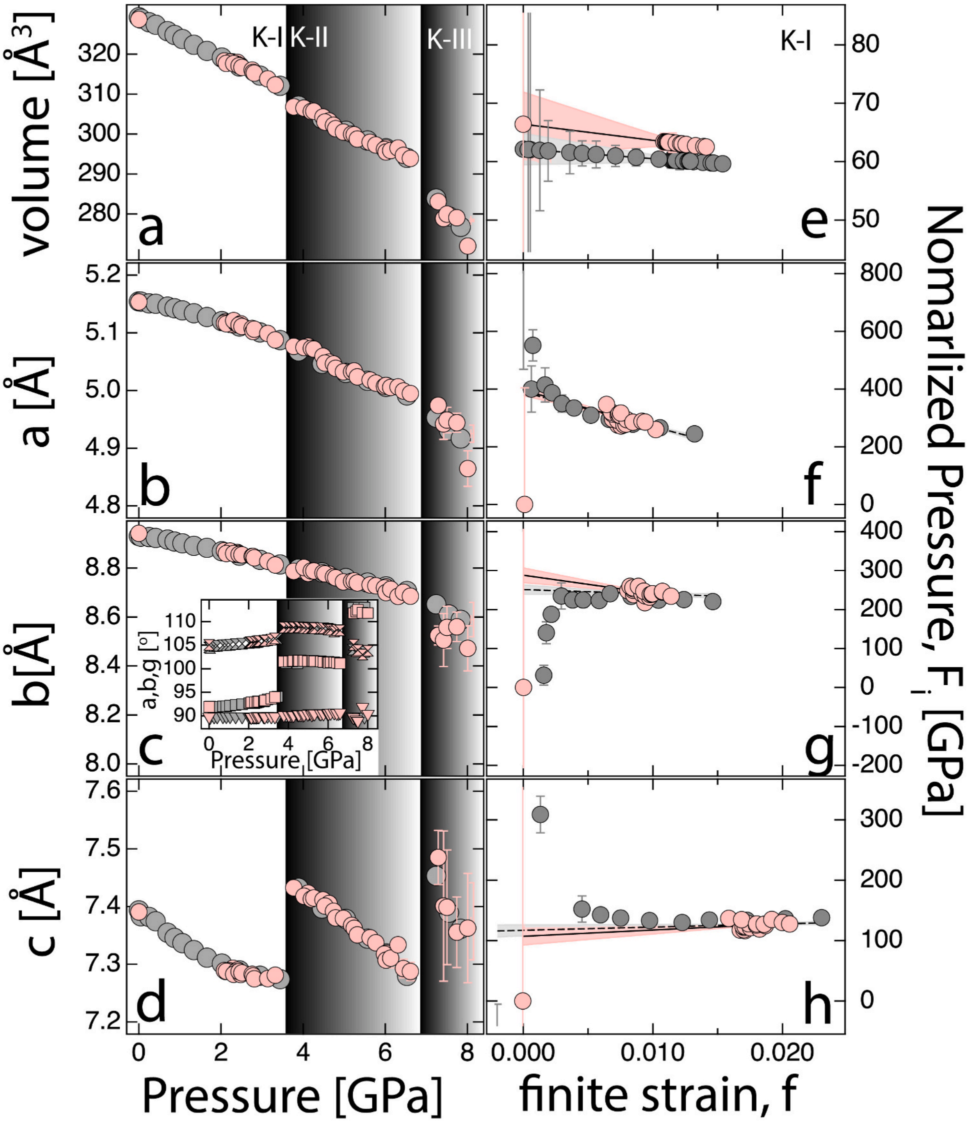

Fig. 6. Equation of state and linear compressibility of the Keokuk kaolinite from synchrotron powder X-ray diffraction measurements at high-pressures (Supplementary Materials). Pressure dependence of (a) unit-cell volume, (b) lattice parameter a, (c) lattice parameter b, (d) lattice parameter c, reveals discontinuous behavior across K-I to K-II and K-II to K-III phase. Inset in (c) shows the pressure dependence of lattice parameters, α, β, and γ. The discontinuous behavior across K-I to K-II and K-II to K-III phase is indicated by dark grey gradational shading. The equation of state of K-I phase is constrained by finite strain formalism eq. (3–8) in the main text. (e) Finite strain (f_v) vs. normalized pressure (F_v) plot. Linear normalized pressure (f_i) vs. linear normalized pressure (F_l) plot for the lattice parameters (f) a (g) b and (h) c respectively. The results are in good agreement with prior study (Welch and Crichton, 2010). The shading represents $\pm 1\sigma$ uncertainty related to finite strain analysis with results from this study (pink) and combining results from this study and prior study (grey) (Welch and Crichton, 2010). (For interpretation of the references to colour in this figure legend, the reader is referred to the web version of this article.)

is of high crystallinity and is free from anatase impurities that is likely to complicate the interpretation of the pressure dependence of the Raman modes in the low energy region. We compressed Keokuk kaolinite and found that the pressure dependence of the hydroxyl modes ν^{OH} was very similar to that have been examined in prior studies with discontinuities at ~3 and ~ 6 GPa. This is related to the polytypic transformation of Kaolinite from K-I to K-II and K-II to K-III phase. Several low-energy Raman modes' pressure dependence also exhibits similar discontinuous behavior. The synchrotron-based powder X-ray diffraction results also indicate discontinuous behavior in the pressure dependence of the unit-cell volume and lattice parameters. The analysis of the bulk and the linear compressibility reveals that kaolinite is extremely anisotropic. Such elastic anisotropy is likely to manifest in unique sets of geophysical signatures, thus likely to be useful in aiding in its detectability. The K-I to K-II polytypic transition is marked by the snapping of hydrogen bonds, thus at conditions relevant to the Earth's interior, aqueous fluid intercalation in the interlayer is likely to stabilize the crystal structure and help form the super-hydrated kaolinite which can transport significantly more water into the Earth's interior.

CRediT authorship contribution statement

Abhisek Basu: Conceptualization, Methodology, Investigation, Formal analysis, Data curation, Validation, Writing – original draft, Writing – review & editing. **Mainak Mookherjee:** Conceptualization, Data curation, Formal analysis, Funding acquisition, Project administration, Resources, Supervision, Writing – original draft, Writing – review & editing. **Stephen Clapp:** Investigation, Formal analysis, Writing – review & editing. **Stella Chariton:** Investigation, Resources, Writing – review & editing. **Vitali B. Prakapenka:** Investigation, Resources, Writing – review & editing.

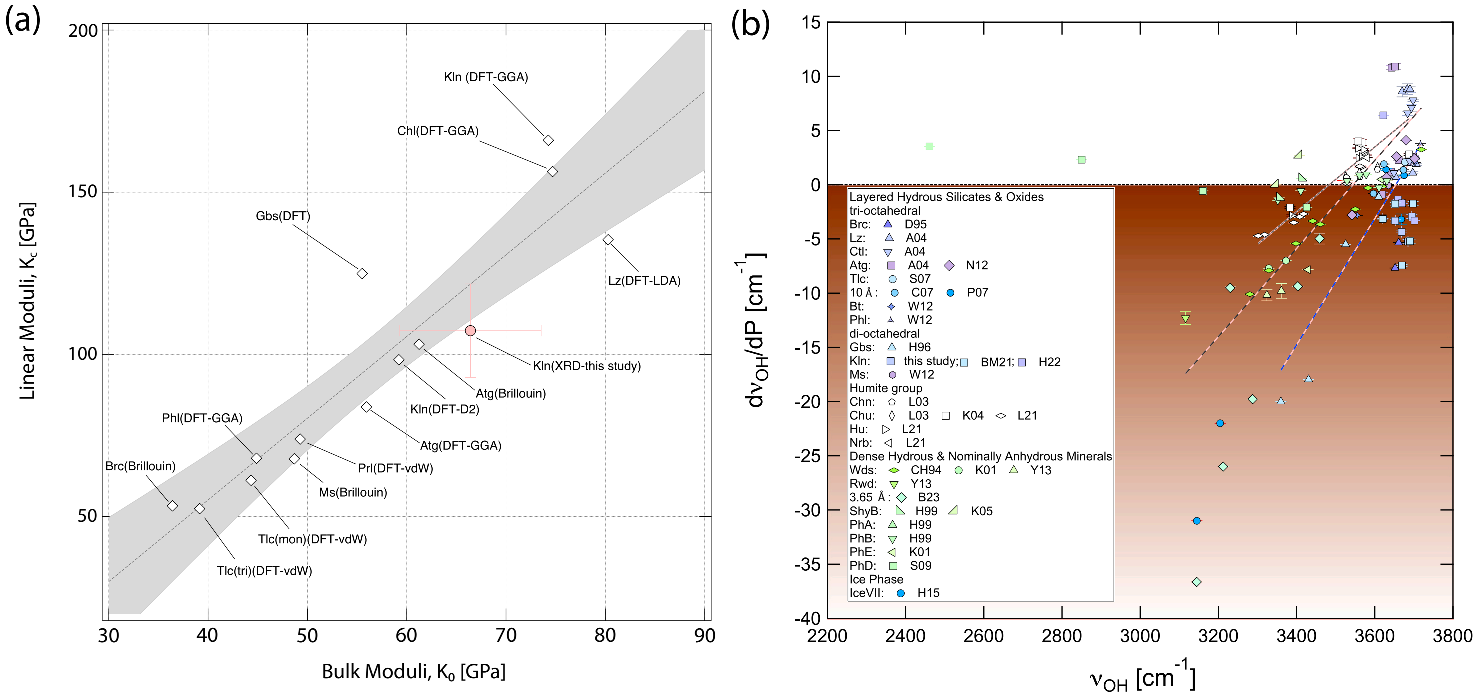

Fig. 7. (a) Correlation between the linear moduli, K_c and the bulk moduli, K_oK$_0$ of selected layered hydrous phase. The line and the shaded band indicate linear correlation and ± 1σ uncertainty respectively. Abbreviations of mineral phases are as follows: brucite (Brc) (Jiang et al., 2006); serpentine polymorph lizardite (Lz) (Mookherjee and Stixrude, 2009) and antigorite (Atg) (Mookherjee and Capitani, 2011; Bezacier et al., 2010); talc (Tlc) (Peng et al., 2022) – mon refers to polytype with monoclinic symmetry and tri refers to the polytype with triclinic symmetry; muscovite (Ms) (Vaughan and Guggenheim, 1986); gibbsite (Gbs) (Gale et al., 2001); phlogopite (Phl) (Chheda et al., 2014); chlorite (Chl) (Mookherjee and Mainprice, 2014); kaolinite (Kln) (this study, Weck et al., 2015) (Supplementary Materials). (b) The pressure dependence of hydroxyl stretching mode frequency, $\frac{d\nu_i^{OH}}{dP}\mathrm{b}_i^{\mathrm{OH}}$ with OH-stretching mode frequency, ν_i^{OH} for several hydrous mineral phases at ambient condition, i.e., 1 bar. Abbreviations for the mineral phases are as follows: trioctahedral: brucite (Brc) – (D95: Duffy et al., 1995); serpentine polymorph lizardite (Lz) – (A04: Auzende et al., 2004), chrysotile (Ctl) – (A04: Auzende et al., 2004), and antigorite (Atg) – (A04: Auzende et al., 2004, N12: Noguchi et al., 2012); talc (Tlc)-(S07: Scott et al., 2007); 10 Å phase – (C07: Comodi et al., 2007, P07: Parry et al., 2007); biotite (Bt) – (W12: Williams et al., 2012); phlogopite (Phl) – (W12: Williams et al., 2012); dioctahedral: gibbsite (Gbs) – (H96: Huang et al., 1996); kaolinite (Kln) – (This study, BM21: Basu and Mookherjee, 2021, H22: Hong 2022); muscovite (Ms) – (W12: Williams et al., 2012); humite group: chondrodite (Chn) – (L03: Liu et al., 2003); clinohumite (Chu) – (L03 and L21: Liu et al., 2003, 2021); humite (Hu) (L21: Liu et al., 2021); norbergite (Nrb) – (L21: Liu et al., 2021); Dense Hydrous Magneisum Phase (DHMS) and Nominally Anhydrous Minerals (NAMs): wadsleyite (Wds) – (CH94: Cynn and Hofmeister, 1994, K01: Kleppe et al., 2001, Y13: Ye et al., 2013); ringwoodite (Rwd) – (Y13: Ye et al., 2013); 3.65 Å phase– (B23: Basu et al., 2023); superhydrous B (ShyB) – (K05: Koch-Müller et al., 2005; H99: Hofmeister et al., 1999); phase A (PhA) – (H99: Hofmeister et al., 1999); phase B (PhB) – (H99: Hofmeister et al., 1999); phase E (PhE) – (K01: Kleppe et al., 2001); phase D (PhD) – (S09: Shieh et al., 2009); ice phase: ice-VII – (H15: Hsieh and Chien, 2015).

Declaration of Competing Interest

The authors declare that they have no known competing financial interests or personal relationships that could have appeared to influence the work reported in this paper.

Data availability

Data will be made available on request.

Acknowledgment

The authors thank Dr. Mark Welch (Natural History Museum, London, UK) for sharing the Keokuk kaolinite sample. MM, AB, and SC acknowledge support from National Science Foundation (EAR1638752; EAR1753125). The X-ray diffraction data were collected at GeoSoilEnviroCARS (Sector 13), Advanced Photon Source (APS), Argonne National Laboratory (ANL). GeoSoilEnviroCARS is supported by the National Science Foundation Earth Sciences award (EAR 1634415). This research used resources from the Advanced Photon Source, a U.S. Department of Energy (DOE) Office of Science User Facility operated for the DOE Office of Science by Argonne National Laboratory (Grant No. DE-AC02-06CH11357).

Appendix A. Supplementary data

Supplementary data to this article can be found online at https://doi.org/10.1016/j.clay.2023.107144.

References

Angel, R.J., 2000. Equations of state. Rev. Mineral. Geochem. 41, 35–59. https://doi.org/10.2138/rmg.2000.41.2.

Angel, R.J., Bujak, M., Zhao, J., Gatta, G.D., Jacobsen, S.D., 2007. Effective hydrostatic limits of pressure media for high-pressure crystallographic studies. J. Appl. Crystallogr. 40, 26–32. https://doi.org/10.1107/S0021889806045523.

Auzende, A.-L., Daniel, I., Reynard, B., Lemaire, C., Guyot, F., 2004. High-pressure behavior of serpentine minerals: a Raman spectroscopic study. Phys. Chem. Miner. 31, 269–277. https://doi.org/10.1007/s00269-004-0384-0.

Balachandran, U., Eror, N.G., 1982. Raman spectra of titanium dioxide. J. Solid State Chem. 42, 276–282. https://doi.org/10.1016/0022-4596(82)90006-8.

Balan, E., Saitta, A.M., Mauri, F., Calas, G., 2001. First-principles modeling of the infrared spectrum of kaolinite. Am. Mineral. 86, 1321–1330. https://doi.org/10.2138/am-2001-11-1201.

Basu, A., Mookherjee, M., 2021. Intercalation of water in kaolinite ($Al_2Si_2O_5(OH)_4$) at subduction zone conditions: insights from Raman spectroscopy. ACS Earth Sp. Chem. 5, 834–848. https://doi.org/10.1021/acsearthspacechem.0c00349.

Basu, A., Chandra, A., Tyagi, A.K., Mukherjee, G.D., 2012. Reappearance of ferroelectric soft modes in the paraelectric phase of $Pb_{1-x}Ca_xTiO_3$ at high pressures: Raman and x-ray diffraction studies. J. Phys. Condens. Mater. 24, 115404. https://doi.org/10.1088/0953-8984/24/11/115404.

Basu, A., Mookherjee, M., Bucag, C., Tkachev, S., Wunder, B., 2023. High-pressure behavior of 3.65 Å phase: insight from Raman spectroscopy. Am. Mineral. 108, 1547–1557. https://doi.org/10.2138/am-2022-8515.

Bezacier, L., Reynard, B., Bass, J.D., Sanchez-Valle, C., Van de Moortèle, B., 2010. Elasticity of antigorite, seismic detection of serpentinites, and anisotropy in subduction zones. Earth Planet. Sci. Lett. 289, 198–208. https://doi.org/10.1016/j.epsl.2009.11.009.

Birch, F., 1978. Finite strain isotherm and velocities for single crystal and polycrystalline NaCl at high-pressures and 300 K. J. Geophys. Res. 83, 1257–1268.

Bish, D.L., 1993. Rietveld refinement of the kaolinite structure at 1.5 K. Clay Clay Miner. 41, 738–744. https://doi.org/10.1346/CCMN.1993.0410613.

Bishop, J.L., Dobrea, E.Z.N., McKeown, N.K., Parente, M., Ehlmann, B.L., Michalski, J.R., Milliken, R.E., Poulet, F., Swayze, G.A., Mustard, J.F., Murchie, S.L., Bibring, J.-P., 2008. Phyllosilicate diversity and past aqueous activity revealed at Mawrth Vallis, Mars. Science 321, 830–833. https://doi.org/10.1126/science.1159699.

Brindley, G.W., Robinson, Keith, 1946. The structure of kaolinite. Mineral. Mag. J. Mineral. Soc. 27, 242–253. https://doi.org/10.1180/minmag.1946.027.194.04.

Chheda, T., Mookherjee, M., Mainprice, D., dos Santos, A.M., Molaison, J.J., Chantel, J., Manthilake, G., Bassett, W.A., 2014. Structure and elasticity of phlogopite under compression: geophysical implications. Phys. Earth Planet. Inter. 233, 1–12. https://doi.org/10.1016/j.pepi.2014.05.004.

Comodi, P., Cera, F., Nazzareni, S., Dubrovinsky, L., 2007. Raman spectroscopy of the 10 Å phase at simultaneously HP-HT. Eur. J. Mineral. 19, 623–629. https://doi.org/10.1127/0935-1221/2007/0019-1753.

Cynn, H., Hofmeister, A.M., 1994. High-pressure IR spectra of lattice modes and OH vibrations in Fe-bearing wadsleyite. J. Geophys. Res. 99, 17717–17727. https://doi.org/10.1029/94JB01661.

Davies, G.F., 1974. Effective elastic moduli under hydrostatic stress-I. quasi-harmonic theory. J. Phys. Chem. Solids 35, 1513–1520.

Dera, P., Prewitt, C.T., Japel, S., Bish, D.L., Johnston, C.T., 2003. Pressure-controlled polytypisim in hydrous layered materials. Am. Mineral. 88, 1428–1435. https://doi.org/10.2138/am-2003-1006.

Duffy, T.S., Meade, C., Fei, Y., Mao, H.-K., Hemley, R.J., 1995. High-pressure phase transition in brucite, $Mg(OH)_2$. Am. Mineral. 80, 222–230. https://doi.org/10.2138/am-1995-3-403.

Ehlmann, B.L., Mustard, J.F., Murchie, S.L., Bibring, J.-P., Meunier, A., Fraeman, A.A., Langevin, Y., 2011. Subsurface water and clay mineral formation during the early history of Mars. Nature 479, 53–60. https://doi.org/10.1038/nature10582.

Farmer, V.C., 1964. Infrared absorption of hydroxyl groups in kaolinite. Science. 145, 11898–1190.

Farmer, V.C., 1974. "The Layer Silicates", The Infrared Spectra of Minerals. V. C. Farmer. https://doi.org/10.1180/mono-4.15.

Farmer, V.C., Russell, J.D., 1964. The infrared spectra of layer silicates. Spectrochim. Acta 20, 1149–1173.

Frost, R.L., 1995. Fourier transform Raman spectroscopy of kaolinite, dickite and halloysite. Clay Clay Miner. 43, 191–195. https://doi.org/10.1346/CCMN.1995.0430206.

Frost, R.L., Kloprogge, J.T., 1999. Raman spectroscopy of the low-frequency region of kaolinite at 298 and 77 K. App. Spetrosc. 53, 1610–1616.

Frost, R.L., van der Gaast, S.J., 1997. Kaolinite hydroxyls- a Raman microscopy study. Clay Miner. 32, 471–484.

Gale, J.D., Rohl, A.L., Milman, V., Warren, M.C., 2001. An ab initio study of the structure and properties of aluminum hydroxide: gibbsite and bayerite. J. Phys. Chem. B 105, 10236–10242. https://doi.org/10.1021/jp011795e.

Gonzales-Platas, J., Rodriguez-Hernandez, P., Muñoz, A., Rodríguez-Mendoza, U.R., Nénert, G., Errandonea, D., 2019. A high-pressure investigation of the synthetic analogue of chalcomenite, $CuSeO_3{\cdot}2H_2O$. Crystals 9, 643. https://doi.org/10.3390/cryst9120643.

Gonzalez-Platas, J., Alvaro, M., Nestola, F., Angel, R., 2016. EosFit7-GUI: a new graphical user interface for equation of state calculations, analyses and teaching. J. Appl. Crystallogr. 49, 1377–1382. https://doi.org/10.1107/S1600576716008050.

Hao, W., Mänd, K., Li, Y., Alessi, D.S., Somelar, P., Moussavou, M., Romashkin, A.E., Lepland, A., Kirsimäe, K., Planavsky, N.J., Konhauser, K.O., 2021. The kaolinite shuttle links the great Oxidation and Lomagundi events. Nat. Commun. 12, 2944. https://doi.org/10.1038/s41467-021-23304-8.

Hazen, R.M., Sverjensky, D.A., Azzolini, D., Bish, D.L., Elmore, S.C., Hinnov, L., Milliken, R.E., 2013. Clay mineral evolution. Am. Mineral. 98, 2007–2029. https://doi.org/10.2138/am.2013.4425.

Heinz, D.L., Jeanloz, R., 1984. The equation of state of the gold calibration standard. J. Appl. Phys. 55, 885–893. https://doi.org/10.1063/1.333139.

Hofmeister, A.M., Cynn, H., Burnley, P.C., Meade, C., 1999. Vibrational spectra of dense, hydrous magnesium silicates at high pressure: Importance of the hydrogen bond angle. Am. Mineral. 84, 454–464. https://doi.org/10.2138/am-1999-0330.

Holtz, M., Solin, S.A., Pinnavaia, T.J., 1993. Effect of pressure on the Raman vibrational modes of layered aluminosilicate compounds. Phys. Rev. B48, 13312–13317. https://doi.org/10.1103/PhysRevB.48.13312.

Hong, M., Dai, L., Hu, H., Zhang, X., 2022. Pressure-induced structural phase transitions in natural kaolinite investigated by Raman spectroscopy and electrical conductivity. Am. Mineral. 107, 385–394. https://doi.org/10.2138/am-2021-7863.

Hsieh, W.-P., Chien, Y.-H., 2015. High-pressure Raman spectroscopy of H_2O-CH_3OH mixtures. Sci. Rep. 5, 8532. https://doi.org/10.1038/srep08532.

Huang, E., Li, A., Xu, J., Chen, R.-J., Yamanka, T., 1996. High-pressure phase transition in $Al(OH)_3$: Raman and X-ray observations. Geophys. Res. Lett. 23, 3083–3086. https://doi.org/10.1029/96GL03023.

Hwang, H., Seoung, D., Lee, Y., Liu, Z., Liermann, H.-P., Cynn, H., Vogt, T., Kao, C.-C., Mao, H.-K., 2017. A role for subducted super-hydrated kaolinite in Earth's deep water cycle. Nat. Geosci. 10, 947–953. https://doi.org/10.1038/s41561-017-0008-1.

Hwang, H., Choi, J., Liu, Z., Kim, D.-Y., He, Y., Celestian, A.J., Voigt, T., Lee, Y., 2019. Pressure-induced hydration and formation of bilayer ice in nacrite, a kaolini-group clay. ACS Earth Sp. Chem. 4, 183–188. https://doi.org/10.1021/acsearthspacechem.9b00255.

Ishii, M., Shimanouchi, T., Nakahira, M., 1967. Far infra-red absorption spectra of layer silicates. Inorg. Chim. Acta 1, 387–392. https://doi.org/10.1016/S0020-1693(00)93207-9.

Jiang, F., Speziale, S., Duffy, T.S., 2006. Single-crystal elasticity of brucite, $Mg(OH)_2$, to 15 GPa by Brillouin scattering. Am. Mineral. 91, 1893–1900. https://doi.org/10.2138/am.2006.2215.

Johnston, C., 1985. Raman spectroscopic study of kaolinite in aqueous suspension. Clay Clay Miner. 33, 483–489. https://doi.org/10.1346/CCMN.1985.0330602.

Johnston, C., 2010. Probing the nanoscale architecture of clay minerals. Clay Miner. 45, 245–279. https://doi.org/10.1180/claymin.2010.045.3.245.

Johnston, C., Wang, S.-L., Bish, D., Dera, P., Agnew, S.F., Kenney, J.W., 2002. Novel pressure-induced phase transformations in hydrous layered materials. Geophys. Res. Lett. 29 https://doi.org/10.1029/2002GL015402, 17–1-4.

Kleppe, A.K., Jephcoat, A.P., Ross, N.L., 2001. Raman spectroscopic studies of phase E to 19 GPa. Am. Mineral. 86, 1275–1281. https://doi.org/10.2138/am-2001-1015.

Kloprogge, J.T., 2017. Raman spectroscopy of clay minerals. In: Developments in Clay Science. Elsevier, pp. 150–199. https://doi.org/10.1016/B978-0-08-100355-8.00006-0.

Klotz, S., Chervin, J.-C., Munsch, P., Le Marchand, G., 2009. Hydrostatic limits of 11 pressure transmitting media. J. Phys. D. Appl. Phys. 42, 075413 https://doi.org/10.1088/0022-3727/42/7/075413.

Koch-Müller, M., Dera, P., Fei, Y., Hellwig, H., Liu, Z., Orman, J.V., Wirth, R., 2005. Polymorphic phase transition in superhydrous phase B. Phys. Chem. Miner. 32, 349–361. https://doi.org/10.1007/s00269-005-0007-4.

Ledoux, R.L., White, J.L., 1966. Infrared studies of hydrogen bonding interaction between kaolinite surfaces and intercalated potassium acetate, hydrazine, formamide, and urea. J. Colloid Interface Sci. 21, 127–152. https://doi.org/10.1016/0095-8522(66)90029-8.

Lisitzin, A.P., Rodolfo, K.S., 1972. Sedimentation in the World Ocean: With Emphasis on the Nature, Distribution and Behavior of Marine Suspensions.

Liu, Z., Lager, G.A., Hemley, R.J., Ross, N.L., 2003. Synchrotron infrared spectroscopy of OH-chondrodite and OH-clinohumite at high pressure. Am. Mineral. 88, 1412–1415. https://doi.org/10.2138/am-2003-1003.

Liu, D., Smyth, J.R., Zhu, X., Miao, Y., Hu, Y., Chen, G., Ye, Y., 2021. High-pressure vibrational spectra of humite-group minerals: fluorine effect on thermodynamic properties and hydrogen bonds. Phys. Earth Planet. Inter. 312, 106654. https://doi.org/10.1016/j.pepi.2021.106654.

Loh, E., 1973. Optical vibrations in sheet silicates. J. Phys. C Solid State Phys. 6, 1091–1104. https://doi.org/10.1088/0022-3719/6/6/022.

Lyons, T.W., Anbar, A.D., Severmann, S., Scott, C., Gill, B.C., 2009. Tracking Euxinia in the Ancient Ocean: a Multiproxy Perspective and Proterozoic Case Study. Annu. Rev. Earth Planet. Sci. 37, 507–534. https://doi.org/10.1146/annurev.earth.36.031207.124233.

Mao, H.K., Xu, J., Bell, P.M., 1986. Calibration of the ruby pressure gauge to 800 kbar under quasi-hydrostatic conditions. J. Geophys. Res. 91, 4673. https://doi.org/10.1029/JB091iB05p04673.

Meade, C., Jeanloz, R., 1990. Static compression of ca$(OH)_2$ at room temperature: observations of amorphization and equation of state measurements to 10.7 GPa. Geophys. Res. Lett. 17, 1157–1160.

Michaelian, K.H., 1986. The Raman spectrum of kaolinite #9 at 21°C. Can. J. Chem. 64, 285–294. https://doi.org/10.1139/v86-048.

Michalski, J.R., Glotch, T.D., Friedlander, L.R., Dyar, M.D., Bish, D.L., Sharp, T.G., Carter, J., 2017. Shock metamorphism of clay minerals on Mars by meteor impact. Geophys. Res. Lett. 44, 6562–6569. https://doi.org/10.1002/2017GL073423.

Mookherjee, M., Capitani, G.C., 2011. Trench parallel anisotropy and large delay times: elasticity and anisotropy of antigorite at high pressures. Geophys. Res. Lett. 38, L09315 https://doi.org/10.1029/2011GL047160.

Mookherjee, M., Mainprice, D., 2014. Unusually large shear wave anisotropy for chlorite in subduction zone settings. Geophys. Res. Lett. 41, 1506–1513. https://doi.org/10.1002/2014GL059334.

Mookherjee, M., Stixrude, L., 2009. Structure and elasticity of serpentine at high-pressure. Earth Planet. Sci. Lett. 279, 11–19. https://doi.org/10.1016/j.epsl.2008.12.018.

Mookherjee, M., Speziale, S., Marquardt, H., Jahn, S., Wunder, B., Koch-Müller, M., Liermann, H.-P., 2015. Equation of state and elasticity of the 3.65 Å phase: implications for the X-discontinuity. Am. Mineral. 100, 2199–2208. https://doi.org/10.2138/am-2015-5312.

Murad, E., 1997. Identification of minor amounts of anatase in kaolins by Raman spectroscopy. Am. Mineral. 82, 203–206. https://doi.org/10.2138/am-1997-1-222.

Neder, R.B., Burghammer, M., Grasl, T.H., Schulz, H., Bram, A., Fiedler, S., 1999. Refinement of the kaolinite structure from single-crystal synchrotron data. Clay Clay Miner. 47, 487–494. https://doi.org/10.1346/CCMN.1999.0470411.

Noguchi, N., Moriwaki, T., Ikemoto, Y., Shinoda, K., 2012. OH group behavior and pressure-induced amorphization of antigorite examined under high pressure and temperature using synchrotron infrared spectroscopy. Am. Mineral. 97, 134–142. https://doi.org/10.2138/am.2012.3904.

Nye, J.F., 1985. Physical Properties of Crystals: Their Representation by Tensors and Matrices. Oxford University Press.

Ohsaka, T., Yamaoka, S., Shimomura, O., 1979. Effect of hydrostatic pressure on the Raman spectrum of anatase (TiO_2). Solid State Commn. 30, 345–347. https://doi.org/10.1016/0038-1098(79)90648-3.

Parry, S.A., Pawley, A.R., Jones, R.L., Clark, S.M., 2007. An infrared spectroscopic study of the OH stretching frequencies of talc and 10 Å phase to 10 GPa. Am. Mineral. 92, 525–531. https://doi.org/10.2138/am.2007.2211.

Pauling, L., 1930. The structure of the micas and related minerals. Proc. Natl. Acad. Sci. 16, 123–129. https://doi.org/10.1073/pnas.16.2.123.

Peng, Y., Mookherjee, M., Hermann, A., Manthilake, G., Mainprice, D., 2022. Anomalous elasticity of talc at high pressures: implications for subduction systems. Geosci. Front. 13, 101381. https://doi.org/10.1016/j.gsf.2022.101381.

Prescher, C., Prakapenka, V.B., 2015. DIOPTAS : a program for reduction of two-dimensional X-ray diffraction data and data exploration. High Pressure Res. 35, 223–230. https://doi.org/10.1080/08957959.2015.1059835.

Railsback, L.B., 2003. An earth scientist's periodic table of the elements and their ions. Geology 31, 737. https://doi.org/10.1130/G19542.1.

Schroeder, P.A., Shiflet, J., 2000. Ti-bearing phases in an East Georgia kaolin deposit. Clay Clay Miner. 48, 151–158.

Schroeder, P.A., Melear, N.D., Pruett, R.J., 2003. Quantitative analysis of anatase in Georgia kaolins using Raman spectroscopy. Appl. Clay Sci. 23, 299–308.

Scott, H.P., Liu, Z., Hemley, R.J., Williams, Q., 2007. High-pressure infrared spectra of talc and lawsonite. Am. Mineral. 92, 1814–1820. https://doi.org/10.2138/am.2007.2430.

Sekiya, T., Ohta, S., Kamei, S., Hanakawa, M., Kurita, S., 2001. Raman spectroscopy and phase transition of anatase TiO_2 under high pressure. J. Phys. Chem. Solids 62, 717–721. https://doi.org/10.1016/S0022-3697(00)00229-8.

Shieh, S.R., Duffy, T.S., Liu, Z., Ohtani, E., 2009. High-pressure infrared spectroscopy of the dense hydrous magnesium silicates phase D and phase E. Phys. Earth Planet. Inter. 175, 106–114. https://doi.org/10.1016/j.pepi.2009.02.002.

Toby, B.H., Von Dreele, R.B., 2013. GSAS-II : the genesis of a modern open-source all purpose crystallography software package. J. Appl. Crystallogr. 46, 544–549. https://doi.org/10.1107/S0021889813003531.

Tosoni, S., Doll, K., Ugliengo, P., 2006. Hydrogen bond in layered materials: structural and vibrational properties of kaolinite by a periodic B3LYP approach. Chem. Mater. 18, 2135–2143. https://doi.org/10.1021/cm060227e.

Vaughan, M.T., Guggenheim, S., 1986. Elasticity of muscovite and its relationship to crystal structure. J. Geophys. Res. 91, 4657–4664. https://doi.org/10.1029/JB091iB05p04657.

Weaver, J.S., 1976. Application of finite strain theory to non-cubic crystals. J. Phys. Chem. Solids 37, 711–718. https://doi.org/10.1016/0022-3697(76)90009-3.

Weck, P.F., Kim, E., Jove-Colon, C.F., 2015. Relationship between crystal structure and thermo-mechanical properties of kaolinite clay: beyond standard density functional theory. Dalton Trans. 44, 12550–12560. https://doi.org/10.1039/C5DT00590F.

Welch, M.D., Crichton, W.A., 2010. Pressure-induced transformations in kaolinite. Am. Mineral. 95, 651–654. https://doi.org/10.2138/am.2010.3408.

Welch, M.D., Montgomery, W., Balan, E., Lerch, P., 2012. Insights into the high-pressure behavior of kaolinite from infrared spectroscopy and quantum-mechanical calculations. Phys. Chem. Miner. 39, 143–151. https://doi.org/10.1007/s00269-011-0469-5.

Williams, Q., Knittle, E., Scott, H., Liu, Z., 2012. The high-pressure behavior of micas: vibrational spectra of muscovite, biotite, and phlogopite to 30 GPa. Am. Mineral. 97, 241–252. https://doi.org/10.2138/am.2012.3824.

Ye, Y., Smyth, J.R., Jacobsen, S.D., Goujon, C., 2013. Crystal chemistry, thermal expansion, and Raman spectra of hydroxyl-clinohumite: implications for water in Earth's interior. Contrib. Mineral. Petrol. 165, 563–574. https://doi.org/10.1007/s00410-012-0823-8.